Power Electronic Systems
Laboratory

Proceedings of the 23rd International Symposium on Power Electronics, Electrical Drives, Automation and Motion (SPEEDAM 2016), Anacapri, Capri, Italy, June 22-24, 2016

Improved Stator Design for an Ultra-High Speed Spinning Ball Motor

M. Schuck,
J. Schäfer,
J. W. Kolar,
D. Steinert

Eidgenössische Technische Hochschule Zürich
Swiss Federal Institute of Technology Zurich

2016
International Symposium on Power Electronics,
Electrical Drives, Automation and Motion

Improved Stator Design for an Ultra-High Speed Spinning Ball Motor

Marcel Schuck, Jannik Schäfer, and Johann W. Kolar
Power Electronic Systems Laboratory, ETH Zurich
8005 Zurich, Switzerland
Email: schuck@lem.ee.ethz.ch

Daniel Steinert
Levitronix GmbH
8005 Zurich, Switzerland

***Abstract*—The ongoing miniaturization trend of electric machines increases the demand for higher rotational speeds to provide a required power level at decreased size. The goal of this project is to push the limits of rotor miniaturization by researching new concepts for bearingless machines with ultra-high rotational speeds exceeding 25 million rotations per minute (Mrpm). Using a simple machine stator consisting of air coils limits the achievable rotor torque, which results in acceleration times of several hours until the aforementioned rotational speeds are reached. This study outlines the torque generation mechanisms of the machine and investigates the stator losses, from which improved stator designs, based on a ferrite core, are derived. The latter significantly increase the motor torque at decreased losses and facilitate fast acceleration of the rotor.**

***Index Terms*—induction machine, magnetic bearing, spinning ball, stator design, ultra-high speed.**

I. Introduction

Increasing the rotational speed of an electric machine allows for decreasing its size for a required power level, thus increasing its power density. This has led to a miniaturization trend of electric drive systems with rising rotational speeds of up to 1 Mrpm [1]. The achievable rotational speeds are mainly limited by friction losses, which need to be reduced to acceptable levels. An effective way of reducing mechanical bearing friction is the contactless levitation of the rotor by magnetic bearings. As the drag acting on the rotor due to air friction increases significantly at high rotational speed, acceleration needs to be performed inside a vacuum to overcome this limitation.

A rotational speed of 23.16 Mrpm has already been reported in 1946 [2] and was achieved with a steel sphere of 0.8 mm in diameter, which was magnetically levitated and accelerated inside a vacuum chamber. At this speed, the ultimate limit, which is imposed by the tensile strength ot the rotor material, was reached and the rotor exploded due to the occurring centrifugal forces. To reach even higher rotational speeds, smaller rotors need to be used to decrease centrifugal loading.

The goal of this project is to push the limits of miniaturization of the rotor with an ultra-high speed motor reaching rotational speeds beyond 25 Mrpm. Ultimately, it is targeted at demonstrating the highest possible rotational speed ever achieved with an electric motor. At the aforementioned scales of the rotors, further limits as imposed by the controllability and precision of the employed magnetic bearing systems need to be overcome to reach this aim. The conducted research helps to extend the limits of electrical machines and to overcome the challenges in regard to power density, mechanical stress and controllability of highly dynamic systems.

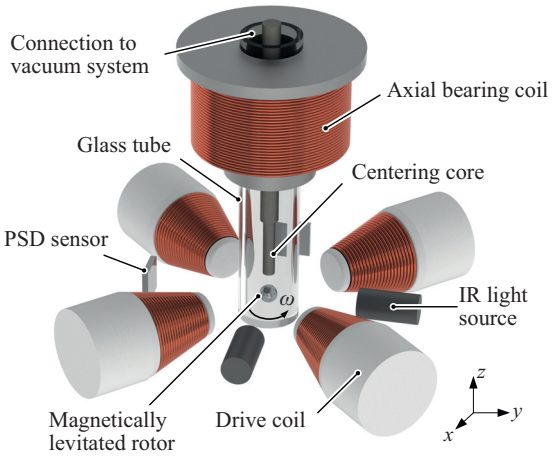

Fig. 1: Setup of the ultra-high speed motor.

The developed motor setup, in which the rotor (a small solid steel sphere) is levitated inside a glass vacuum tube by an axial active magnetic bearing (AMB), is shown in Fig. 1. It is accelerated by the magnetic field which is generated by four radially-placed drive coils based on the principle of a solid rotor induction machine [4]. These coils are also used to implement an AMB in radial direction by superimposing the bearing currents onto the high frequency (≤ 1 MHz) drive currents. The rotor position is measured optically in all three dimensions and the control is implemented digitally by using an FPGA for sufficient bandwidth. For simplicity and to avoid high frequency core losses, air coils have been used for the stator in the past. However, the achievable rotor torque is very small, causing the acceleration to rotational speeds of 25 Mrpm to take several hours, during which the rotor has to be stably levitated and external disturbances need to be avoided.

This paper presents improved stator topologies which use a ferrite core and overcome the aforementioned limitations by allowing acceleration of the rotor within minutes at decreased losses. Before outlining the design process and providing a comparative analysis of the different topologies, the underlying mechanism of torque generation and the drive current

978-1-5090-2067-6/16/$31.00 ©2016 IEEE

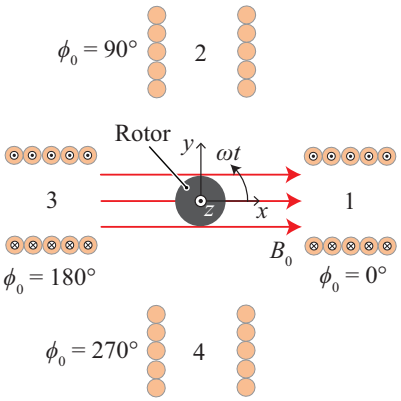

Fig. 2: Magnetic field of the drive coils for torque generation.

modulation scheme are described briefly. Moreover, analytical models for calculating the occurring stator losses are provided.

II. Torque Generation

A torque is exerted on the rotor of the solid rotor induction machine due to the interaction of eddy currents flowing inside the sphere with the external magnetic flux density $\vec{B}$. The latter can be approximated by a rotating vector of magnitude B_0 and is generated by the drive coils as schematically shown in Fig. 2. The slip frequency is denoted by ω and is the difference of the mechanical angular rotating frequency of the rotor ω_r and the angular frequency of the magnetic field ω_f. To generate a rotating field, the currents in the coils denoted by 2, 3, and 4 are phase shifted with respect to the current in coil 1. In the depicted case, the field vector is pointing in the $+x$ direction, corresponding to the instant when the currents in coils 1 and 3 reach their maximum and minimum values, respectively, while the currents in coils 2 and 4 are zero.

The rotor torque in such a setup has been analyzed in detail in [5] and can be expressed as

$$\vec{T} = \underbrace{\frac{3\pi a^3}{1+\sqrt{2}}\frac{B_0^2}{\mu_0}}_{T_\mathrm{bd}} \underbrace{\frac{2+\sqrt{2}}{\sqrt{2}+\frac{C_\mathrm{s}}{\sqrt{\mu_0\omega}}+\frac{\sqrt{\mu_0\omega}}{C_\mathrm{s}}}}_{\xi} \vec{e}_z, \tag{1}$$

where a denotes the rotor radius. The breakdown torque denoted by T_bd is the maximum achievable torque for a given rotor radius and magnetic flux density, which is scaled by the factor ξ dependent on the rotor properties and the slip frequency. The sphere constant C_s contains the characteristic rotor parameters and is given as

$$C_\mathrm{s} = \frac{1}{a}\sqrt{\frac{\mu_r}{\sigma}}, \tag{2}$$

where μ_r and σ denote the relative permeability and the electrical conductivity of the rotor material, respectively. A rotor material typically used in the experiments is the chrome steel 100Cr6 ($\mu_r \approx 4, \sigma \approx 4.5$ MS/m), yielding $C_\mathrm{s} \approx 1.7 \times 10^3$.

The angular acceleration of the spherical rotor with given mass moment of inertia I is described by the relation

$$\dot{\omega}_\mathrm{r} = \frac{T}{I}. \tag{3}$$

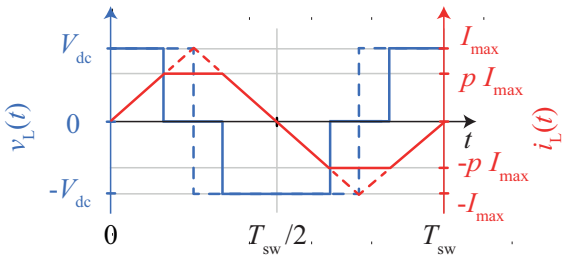

Fig. 3: Output voltage (blue) and current (red) for a full-bridge inverter in block commutation.

Consequently, to achieve fast angular acceleration of the rotor, a high torque is desirable. This can be accomplished for a given rotor size and material by

1) optimizing the magnitude of the flux density B_0 at the rotor for high values to achieve a high breakdown torque,

2) choosing ω such that a scaling factor as close to 1 as possible is obtained.

Option 1 is constrained by how well the magnetic flux density of the drive coils can be guided towards the rotor and the achievable drive current. Option 2 is constrained by the fact that ω_f, and consequently the frequency of the drive currents, has to be higher than the desired rotational speed. In both cases, the stator and rotor losses represent an upper bound, while the latter are usually more critical due to the lack of contact-based cooling possibilities.

III. Drive Current Modulation

The torque model of (1) is based on the assumption of a uniformly rotating external flux density vector $\vec{B}$, which corresponds to sinusoidal drive currents. To achieve rotational speeds exceeding 25 Mrpm, a magnetic field with a frequency $f_\mathrm{f} > 400$ kHz and drive currents of equally high frequency are required. For such frequencies it is cumbersome to generate sinusoidal currents, as the desired output frequency is in the range of the switching frequency f_sw of the power electronic converter and common modulation schemes, such as described in [6], cannot be used. Instead, a standard full-bridge inverter is used in fundamental frequency commutation. The obtainable discrete voltage levels across the coils are $+V_\mathrm{dc}$, $-V_\mathrm{dc}$, and 0 V, with V_dc denoting the dc-link voltage. The resulting output voltage and current waveforms are displayed in Fig. 3. The coil current is directly related to the voltage at the terminals of the drive coil with inductance L as

$$i_L(t) = \frac{1}{L}\int v_L(t)\mathrm{d}t, \tag{4}$$

where the dc resistance of the coil has been neglected. Consequently, the achievable peak current magnitude is given as

$$I_\mathrm{max} = \frac{V_\mathrm{dc}}{2Lf_\mathrm{sw}}, \tag{5}$$

where the frequency of the output current is equal to the switching frequency. If saturation effects are neglected, which

is adequate for the flux densities at hand (see Section V), the relation

$$B_0 \propto I_{\max} \tag{6}$$

holds, which illustrates that for a given V_{dc} the inductance L should be small in order to achieve a high current and, consequently, a high flux density at the rotor.

To employ the model of (1) for the obtained non-sinusoidal drive currents, a Fourier series-based analysis of the currents is performed to assess the contribution of each harmonic component to the torque generation. The waveform as shown in Fig. 3 (red) can be represented by

$$x_{\mathrm{tri}}(t) = \begin{cases} \frac{2A}{\pi} t & t \in \left[0, p\frac{\pi}{2}\right] \\ pA & t \in \left[p\frac{\pi}{2}, \left(1-\frac{p}{2}\right)\pi\right] \\ pA - \frac{2A}{\pi}\left[t - \left(1-\frac{p}{2}\right)\pi\right] & t \in \left[\left(1-\frac{p}{2}\right)\pi, \pi\right] \end{cases} \tag{7}$$

in the time domain, where the factor $p \in (0, 1]$ scales the maximum amplitude A, which is equivalent to $I_{\max}$. The coefficients of the Fourier series are calculated for its standard notation

$$x(t) = \frac{a_0}{2} + \sum_{k=1}^{\infty} \left[a_k \cos(k(\omega_0 t - \phi_0)) + b_k \sin(k(\omega_0 t - \phi_0))\right], \tag{8}$$

where k, ω_0, and ϕ_0 denote the harmonic order, the fundamental frequency corresponding to $2\pi f_{\mathrm{sw}}$, and a phase shift angle, respectively. The function has zero average value and is odd, resulting in $a_0 = 0$ and $a_k = 0$. The coefficients b_k have been derived as

$$b_k = \frac{4A}{(\pi k)^2}\left[\sin\left(kp\frac{\pi}{2}\right) - \sin(k\pi) - \sin\left(n(p-2)\frac{\pi}{2}\right)\right], \tag{9}$$

which is equal to the standard triangular waveform for $p = 1$.

A positive contribution of the k^{th} harmonic component to the overall torque is obtained if $b_k > 0$, which corresponds to $\vec{B}$ rotating in counterclockwise (mathematically positive) direction. Contrarily, $b_k < 0$ corresponds to $\vec{B}$ rotating in negative direction for the considered harmonic, thus generating a decelerating torque. By taking (1) and (6) into account, a figure of merit (FOM) can be defined as

$$\mathrm{FOM} \propto \sum_{k=1}^{N} \mathrm{sgn}(b_k) \cdot b_k^2 \cdot \xi \tag{10}$$

to assess the dependency of the rotor torque on p. The value of this sum, evaluated up to $N = 20$ and normalized to its maximum value at $p = 1$, is shown in Fig. 4 for varying values of p. The maximum torque is achieved for $p = 1$ as expected. Decreasing p to 0.8, and thereby reducing the peak magnitude of the drive current by 20 % and the occurring core losses by almost 40 % (see Section IV), corresponds to a decrease in torque of less than 10 % and can, therefore, be beneficial.

IV. Stator Losses

Losses in the drive system occur in the stator and the rotor. Yet, an improved stator design can be developed independently of rotor loss limitations by considering the achievable torque relative to the resulting stator losses. For stator topologies with obtainable operating conditions exceeding the allowable rotor losses, the drive currents can be reduced to maintain an allowable operating range.

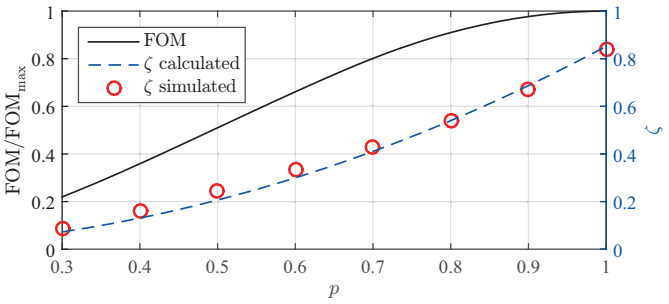

Fig. 4: Normalized FOM for varying values of p as well as calculated and simulated scaling of overall stator core losses (see Section IV for explanation).

In a stator consisting of air coils, the only occurring losses are conduction losses in the employed copper windings. Additional losses occur if a ferromagnetic core is used, which can be subdivided into hysteresis losses, eddy current losses, and residual losses, such as resonance losses [7].

A. Copper Losses

The average ohmic losses originating from the resistance R_{c} of the drive coil can be obtained as

$$P_{\mathrm{r}} = \overline{p_{\mathrm{r}}(t)} = \frac{R_{\mathrm{c}}}{T_{\mathrm{sw}}} \int_{t_0}^{t_0+T_{\mathrm{sw}}} i_L^2(t)\mathrm{d}t. \tag{11}$$

They can equivalently be calculated based on the provided harmonic analysis as

$$P_{\mathrm{r}} = R_{\mathrm{c}} \cdot \sum_{k=1}^{\infty} \frac{b_k^2}{2}, \tag{12}$$

which makes it possible to analyze the contribution of each harmonic component.

The overall resistance R_{c} of the drive coil is comprised of its dc resistance R_{dc} and its ac resistance R_{ac}, where the latter is caused by the skin and proximity effects

$$R_{\mathrm{c}} = R_{\mathrm{dc}} + R_{\mathrm{ac,skin}} + R_{\mathrm{ac,prox}}. \tag{13}$$

R_{dc} is calculated as

$$R_{\mathrm{dc}} = \frac{4l}{\sigma_{\mathrm{w}} \pi d_{\mathrm{w}}^2}, \tag{14}$$

with l, σ_{w}, and d_{w} being the length of the used coil wire, its conductivity, and its diameter, respectively. Detailed models for estimating the ac losses have been presented in the literature [8], [9]. For the construction of the ultra-high speed motor, litz wire is used, which has a higher dc resistance than a single copper wire of equal overall diameter but effectively minimizes the contribution of the ac resistances to negligible levels. Thus, the overall coil resistance can be approximated

TABLE I: Ferrite 3C90 Material Characteristics

Parameter	μ_i	C	α	β
Value	≈ 2300	0.94	1.52	2.68

as

$$R_\mathrm{c} \approx R_\mathrm{dc}. \tag{15}$$

B. Core Losses

Using a ferromagnetic stator core is beneficial as it offers the possibility to guide the flux density toward the rotor. Moreover, it reduces electromagnetic compatibility (EMC) issues by decreasing stray fields.

For the required frequencies of the drive field in the range of several hundreds of kilohertz, a stator core made from ferrite material is the only feasible option. Other core materials, such as laminated steel, which are commonly used in standard electrical machines, would suffer from excessive eddy current and hysteresis losses at such high frequencies. For the subsequent analyses, the example ferrite core material Ferroxcube 3C90 [10] is considered, as it was available in suitable geometries for implementing the desired stator geometries. Generally, many other ferrite materials are available with similar properties, and the choice about which material is most suitable has to be made based on the occurring frequency and magnitude of the flux density, as well as the temperature of the core.

The overall losses for a core volume V_c can be modeled by the Steinmetz equation for various materials

$$P_\mathrm{c,SE} = V_\mathrm{c} C f_\mathrm{s}^\alpha B_\mathrm{s,pk}^\beta, \tag{16}$$

where C, α, and β are material-dependent Steinmetz parameters. These have been calculated from the datasheet of the 3C90 material and are listed in Tab. I, where μ_i denotes the initial relative permeability. The frequency and peak magnitude of the magnetic flux density are denoted by f_s and $B_\mathrm{s,pk}$, respectively. The relation of (16) is only valid for sinusoidal variations of the magnetic flux density and excitation currents. As the currents vary in a non-sinusoidal manner in the considered case, a generalized model has to be used. The improved general Steinmetz equation (iGSE) considers arbitrary variations of the flux and is given as [11]

$$P_\mathrm{c,iGSE} = V_\mathrm{c} C_\mathrm{i} f_\mathrm{s} (\Delta B)^{\beta-\alpha} \cdot \int_0^{T_\mathrm{s}} \left| \frac{\mathrm{d}B}{\mathrm{d}t} \right|^\alpha \mathrm{d}t, \tag{17}$$

where ΔB denotes the peak-to-peak variation of the magnetic flux density and T_s is the period of its variation. The absolute value of the derivative $|\mathrm{d}B/\mathrm{d}t|$ considers increased core losses due to high slew rates. The constant C_i is related to the previously considered Steinmetz parameters by

$$C_\mathrm{i} = \frac{C\sqrt{\pi}}{(2\pi)^\alpha \cdot 2^{\beta-\alpha}} \cdot \frac{\Gamma\left(\frac{2+\alpha}{2}\right)}{\Gamma\left(\frac{1+\alpha}{2}\right)}, \tag{18}$$

where Γ denotes the gamma function. For the trapezoidal current and flux waveforms, as discussed in Sec. III, this yields

$$P_\mathrm{c,iGSE} = V_\mathrm{c} C_\mathrm{i} p (2B_\mathrm{t,pk})^{\beta-\alpha} \left(\frac{4 f_\mathrm{s} B_\mathrm{t,pk}}{p} \right)^\alpha. \tag{19}$$

To assess the influence of the non-sinusoidal excitation on the overall core losses, the ratio

$$\zeta = \frac{P_\mathrm{c,iGSE}}{P_\mathrm{c,SE}} \tag{20}$$

has been calculated for $B_\mathrm{t,pk} = B_\mathrm{s,pk}$. This corresponds to an identical peak value of the sinusoidal waveform, as used for comparison, to the maximum occurring value of the trapezoidal waveform. By using ζ as a correction factor, the core losses can be calculated analytically for the occurring waveforms based on the well-documented material properties for sinusoidal excitation. The ratio ζ is displayed in Fig. 4 for different values p. It can be observed that the overall core losses are lower for the trapezoidal waveform than for a sinusoidal waveform with identical peak magnitude. The calculations are in good agreement with the values as obtained by transient 3D FEM electromagnetic simulations. Slight deviations, particular at low values of p, result from an underestimation of the losses by the iGSE, as it neglects losses due to dc bias and relaxation effects. Analytic models for taking these losses into account have been presented in the literature [12] but require additional modeling complexity.

V. Stator Design

The goal of the improved stator design is to generate a high motor torque, which can be achieved by generating a high flux density magnitude at the rotor. A design only consisting of air coils, such as displayed in Fig. 1, is considered first, followed by two designs with ferrite cores.

A. Air Coil Design

An advantage of air coils is their relatively low inductance value as compared to a design comprising a ferromagnetic core. This allows for high drive currents, even with limited available dc-link voltage. To maximize the flux density at the rotor, a conical coil shape, such as displayed in the inset of Fig. 5, is chosen in which the individual windings are located closer to the rotor than with a cylindrical coil. Yet, the increased radii of the windings which are located further away from the rotor also increase their inductance values. Exact analytic solutions for the magnetic field as generated by conical helix coils have been presented in the literature [13]. However, these results do not allow for an analytic assessment of the problem due to their complexity. Therefore, the coil is approximated by multiple separated concentric loops. The magnitude of the flux density along the axis of the coil, as generated by these loops, can be calculated by the Biot-Savart law as

$$B_{\mathrm{a},n} = \frac{\mu_0 \cdot i_l \cdot r_n^2}{2(l_n + r_n^2)^{3/2}}, \tag{21}$$

where i_l, r_n, and l_n denote the current flowing in the loop, the radius of the loop, and the distance from the center of the

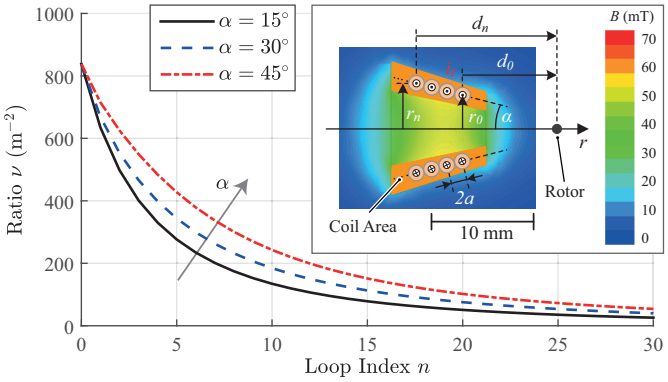

Fig. 5: Ratio ν for the n^{th} winding and geometrical parameters for the conical air coil design with distribution of the magnetic flux density (inset).

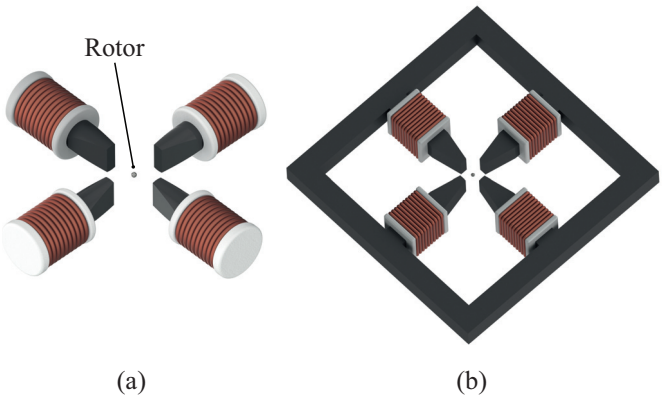

Fig. 6: Stator designs with cylindrical ferrite rods (a) and ferrites with square cross section and back iron (b).

loop to the center of the rotor for the n^{th} loop, respectively. The inductance of a single loop can be approximated by [14]

$$L_n \approx \mu_0 r_n \left[\ln\left(\frac{8r_n}{r_{\text{w}}}\right) - 2 \right], \tag{22}$$

where r_{w} denotes the wire radius. If multiple loops are combined to a conical coil, the distances to the center of the sphere and the radii of the individual loops are obtained as

$$r_n = r_0 + 2a \cdot n \cdot \sin(\alpha) \tag{23a}$$

$$d_n = d_0 + 2a \cdot n \cdot \cos(\alpha), \tag{23b}$$

where r_0 and d_0 denote the radius and distance of the first loop and α is the semiangle of the cone. The minimum distance d_0 is determined by the requirements of the setup, such as the geometry of the optical path for the position sensors and the vacuum system, and should be chosen as small as possible. For each ring n, the ratio $\nu = B_{\text{a},n}/(i_l \cdot L_n)$, which relates the generated flux density at the rotor to the inductance of the winding, has been calculated for different values of α. The results are shown in Fig. 5, which illustrates that ν decreases for windings which are further away from the rotor, as expected. This decrease is less rapid for higher values of α.

For the practical implementation, a compromise between high flux density at the rotor, low inductance, and relatively low coil current was found by implementing a conical coil with a semiangle of 15° and three layers of 15 windings each.

The resulting flux density distribution has been obtained for a magnitude of $B_0 = 5$ mT at the center of the motor, without the rotor in place, by 3D FEM simulation and is displayed in the inset of Fig. 5. A rotor of 1 mm in diameter has been added to the figure for size comparison.

B. Ferrite Core Design

By inserting a ferrite core into the center of the drive coils, the coil inductance is significantly increased due to the high relative permeability μ_r of the core material. This decreases the achievable drive current, but a significantly better guidance of the magnetic flux toward the rotor is achieved. Based on (16) and (17), it is apparent that the core volume should be kept as small as possible to limit the volume-proportional core losses. At the same time, the volume has to be sufficiently large for guiding the magnetic flux without saturation due to field elevations and to guarantee mechanical stability.

The two considered designs which use a ferrite core are shown in Fig. 6, where a spherical rotor of 1 mm in diameter has been added for size comparison. Particular attention was paid to the producibility of the designs, as ferrite material is very brittle and, therefore, difficult to machine. The first design without a back iron is based on commercially available ferrite rods of 6 mm in diameter and 25 mm in length, which are inserted into cylindrical coils. A flat area was ground to the sides of the rods, as shown in Fig. 6(a), yielding a width of the stator teeth facing the rotor of 2 mm. This concentrates the magnetic field close to the rotor and increases the air gap between adjacent poles, thus decreasing short-circuiting of the magnetic field. The height of the stator teeth facing the rotor of 6 mm ensures a constant torque for different axial rotor positions. The distance between two opposite poles has been chosen such that sufficient space for the vacuum tube and the sensors is provided. The second design, as shown in Fig. 6(b), including a back iron is based on ferrites with a square cross-section of 6×6 mm and 25 mm in length. The poles have the same geometry as in the first design and the back iron was assembled by stacking multiple ferrites. The back iron allows the flux lines of the magnetic field to close inside the high permeability stator material rather than the surrounding air, which yields a further increase of the flux density magnitude at the rotor.

VI. Comparative Analysis

In order to select the most suitable stator design for the ultra-high speed motor, a comparative analysis of the previously demonstrated designs is carried out. The assessment is performed based on the achievable magnitude of the magnetic flux density at the rotor per required coil current and occurring stator losses.

For this purpose, the different stator designs have been analyzed using 3D FEM simulations. The achievable magnitude of the magnetic flux density per stator current in ampere-turns

TABLE II: Comparison of characteristic values for the stator designs - refer to text for explanation

	Air Coils	Individual Ferrite Cores	Ferrite Cores with Yoke
a)	9.17 µT/AT	73.6 µT/AT	255.7 µT/AT
b)	10.1 pNm	1.1 nNm	14.3 nNm

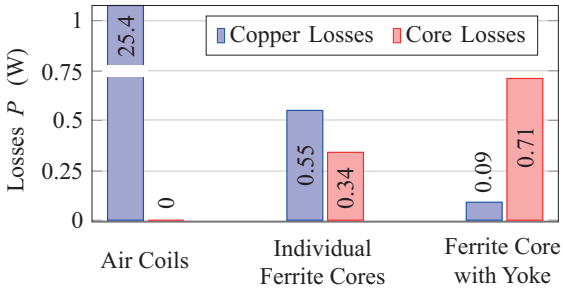

Fig. 7: Comparison of losses for the different stator designs.

(AT) at the center of the motor has been obtained and is listed in row a) of Table II. These simulations were carried out without the rotor in place to exclude its influence on the flux density. It can be seen that the lowest ratio is obtained by the air coil design, while a significant improvements can be achieved by using ferrite cores.

In a second step, the occurring stator losses were studied using eddy current simulations at a drive frequency of $f_s = 500$ kHz, corresponding to a synchronous rotational speed of 30 Mrpm. To allow for easy comparability of the results, the simulations were carried out for a flux density magnitude of $B_0 = 5$ mT at the center of the motor (see Section V) for all designs. The results are shown in Fig. 7, where the conduction losses have been obtained by using a conductivity for copper of 58 MS/m and the currents have been assumed to be evenly distributed over the winding windows of the stator coils (see inset of Fig. 5). The practically encountered losses will likely be higher, due to fill factor limitations and higher resistance of the employed litz wire. Nevertheless, good relative correctness for comparison of the designs is obtained. It is apparent that the overall losses can be significantly reduced with the ferrite core designs and that the set operating conditions are likely unattainable with the air coil design, due to excessive copper losses. In accordance with the listed value of row a) in Table II, a current of about 545 AT is required in the air coils to obtain $B_0 = 5$ mT. Moreover, it can be seen that the losses are shifted towards the core for the design with the back iron (higher core volume) in comparison to the design using individual ferrite cores. However, the overall losses are within the same range.

It should be noted that the outlined losses were obtained for sinusoidal drive currents, which is sufficient to provide a relative correctness of the values, and have to be scaled dependent on the actual current waveform and value of p as outlined in Section IV.

To provide a comparison of the achievable drive torque for operating conditions that are attainable for all presented designs, eddy current simulations have also been carried out for a coil current of 25 AT in all designs. The results are listed in row b) of Table II, and demonstrate a significant increase of the drive torque (without taking any breaking torques into account), which results from the quadratic dependency of the torque on the magnitude of the magnetic flux density as outlined in (1).

VII. Conclusion

The relevant models for developing an improved stator design for an ultra-high speed motor have been presented. One stator design based on air coils and two designs based on ferrite cores have been considered and evaluated through 3D FEM simulations. It has been shown that designs using a ferrite core are favorable, as they feature higher achievable drive torque while significantly reducing the overall stator losses. The use of ferrite-core-based stator topologies for ultra-high speed machines has not widely been considered in the literature and exceeds the scope of [2], [4]. The obtained results are universally applicable and facilitate acceleration of the rotor in the considered ultra-high speed motor to rotational speeds beyond 25 Mrpm within minutes instead of hours.

Acknowledgment

The authors would like to thank the Else & Friedrich Hugel Fund for Mechatronics for supporting this work.

References

[1] C. Zwyssig, J. Kolar, and S. Round, "Megaspeed drive systems: Pushing beyond 1 million r/min," *IEEE/ASME Trans. Mechatronics*, vol. 14, no. 5, pp. 564–574, 2009.

[2] J. W. Beams, J. L. Young, and J. W. Moore, "The production of high centrifugal fields," *Journal of Applied Physics*, vol. 17, no. 11, pp. 886–890, 1946.

[3] A. Boletis and H. Bleuler, "Achieving ultra-high rotating speeds," in *8th International Symposium on Magnetic Bearing, Mito, Japan*, 2002, pp. 539–542.

[4] C. Wildmann, T. Nussbaumer, and J. Kolar, "10 mrpm spinning ball motor: Preparing the next generation of ultra-high speed drive systems," in *Power Electronics Conference (IPEC), 2010 International*, 2010, pp. 278–283.

[5] T. Reichert, T. Nussbaumer, and J. W. Kolar, "Complete analytical solution of electromagnetic field problem of high-speed spinning ball," *Journal of Applied Physics*, vol. 112, no. 10, pp. –, 2012.

[6] D. G. Holmes and T. A. Lipo, *Pulse width modulation for power converters: principles and practice*. John Wiley & Sons, 2003, vol. 18.

[7] A. Moulson and J. Herbert, "Electronic ceramic materials and their applications," *Chapman and Hall, London*, 1990.

[8] W. Hurley, E. Gath, and J. Breslin, "Optimizing the AC resistance of multilayer transformer windings with arbitrary current waveforms," *IEEE Trans. Power Electron.*, vol. 15, no. 2, pp. 369–376, 2000.

[9] X. Nan and C. Sullivan, "Simplified high-accuracy calculation of eddy-current loss in round-wire windings," in *Power Electronics Specialists Conference, 2004. PESC 04. 2004 IEEE 35th Annual*, vol. 2, 2004, pp. 873–879.

[10] *3C90 Material specification*, Ferroxcube, 9 2008.

[11] K. Venkatachalam, C. Sullivan, T. Abdallah, and H. Tacca, "Accurate prediction of ferrite core loss with nonsinusoidal waveforms using only steinmetz parameters," in *Computers in Power Electronics, 2002. Proceedings. 2002 IEEE Workshop on*, 2002, pp. 36–41.

[12] J. Muhlethaler, J. Biela, J. Kolar, and A. Ecklebe, "Core losses under the DC bias condition based on steinmetz parameters," *IEEE Trans. Power Electron.*, vol. 27, no. 2, pp. 953–963, 2012.

[13] L. Holmes, "Stability of magnetic levitation," *Journal of Applied Physics*, vol. 49, no. 6, pp. 3102–3109, 1978.

[14] R. S. Elliot, *Electromagnetics: history, theory, and applications*. IEEE, 1993.